International Journal of Remote Sensing
Vol. 26, No. 15, 10 August 2005, 3137–3148

Taylor & Francis
Taylor & Francis Group

De-shadowing of satellite/airborne imagery

R. RICHTER* and A. MÜLLER
DLR, German Aerospace Center, Remote Sensing Data Center, D-82234 Wessling, Germany

(*Received 2 March 2004; in final form 23 December 2004*)

A de-shadowing technique is presented for multispectral and hyperspectral imagery over land acquired by satellite/airborne sensors. The method requires a channel in the visible and at least one spectral band in the near-infrared (0.8–1 μm) region, but performs much better if bands in the short-wave infrared region (around 1.6 and 2.2 μm) are available as well. The algorithm consists of these major components: (i) calculation of the covariance matrix and zero-reflectance matched filter vector, (ii) derivation of the unscaled and scaled shadow function, (iii) histogram thresholding of the unscaled shadow function to define the core shadow areas, (iv) region growing to include the surroundings of the core shadow areas for a smooth shadow/clear transition, and (v) de-shadowing of the pixels in the final shadow mask. The critical parameters of the method are discussed. Example images from different climates and landscapes are presented to demonstrate the successful performance of the shadow removal process over land surfaces.

1. Introduction

Remotely sensed optical imagery of the Earth's surface is often contaminated with cloud and cloud shadow areas. Surface information under cloud-covered regions cannot be retrieved with optical sensors, because the signal contains no radiation component being reflected from the ground. In shadow areas, however, the ground-reflected solar radiance is always a small non-zero signal, because the total radiation signal at the sensor contains a direct (beam) and a diffuse (reflected skylight) component. Even if the direct solar beam is completely blocked in shadow regions, the reflected diffuse flux will remain. Therefore, an estimate of the fraction of direct solar irradiance for a fully or partially shadowed pixel can be the basis of a compensation process called de-shadowing or shadow removal.

The method presented here is restricted to land areas and works only for scenes with a cloud cover of less than about 25%. Although the results of shadow removal in terms of derived surface reflectance cannot be expected to be as accurate as clear-sky reflectance imagery, the enhanced display of surface features and the shadow-corrected surface reflectance spectra are a valuable source of information in multitemporal monitoring applications.

Several de-shadowing techniques have been described in the literature. One approach employs geometric considerations to project the cloud structure on the ground based on the direction of the incident solar radiation and the estimated cloud height (Simpson and Stitt 1998). Another employs unmixing of

*Corresponding author. E-mail: rudolf.richter@dlr.de

International Journal of Remote Sensing
ISSN 0143-1161 print/ISSN 1366-5901 online © 2005 Taylor & Francis
http://www.tandf.co.uk/journals
DOI: 10.1080/01431160500114664

atmospherically corrected data (Boardman 1993) using the concept of spectral endmembers. Shadow is defined as a zero-reflectance endmember, and the sum of all endmember weights is constrained to 1. After unmixing, the de-shadowing operation divides the reflectance by 1 minus the sum of the non-shadow endmember weights. Problems with this approach include the dependence of the results on the choice of endmembers and the neglection of the diffuse skylight. A third approach uses the matched filter concept (Adler-Golden *et al*. 2002), where the matched filter vector is calculated in terms of the covariance matrix of the atmospherically corrected reflectance data. The matched filter concept itself has been applied in other technical fields as well, e.g. information technology and signal processing (Turin 1975, 1976, Poor 1983).

This contribution also employs the matched filter concept as one step of the de-shadowing method. The application of the matched filter vector to the atmospherically corrected reflectance imagery yields unscaled, positive and negative shadow abundance values. However, the re-scaling of the unscaled function into the physical interval (0,1), containing the fraction of direct illumination, is performed with a new strategy, as detailed in the next section.

All mentioned spectral methods imply the independence of pure spectra. This may not be true, especially in complex scenes. So misclassifications do occur. As an example, a fully illuminated pixel of a dark material can be classified as a shadowed pixel of another material or combination of materials. Still, useful de-shadowed images have been processed for a variety of different climatic and landscape conditions. The concept of core shadow areas, proposed here, substantially reduces the number of misclassifications in most imagery as compared to the standard approach.

2. Outline of de-shadowing method

The method starts with a calculation of the surface reflectance image cube $\rho_i = \rho(\lambda_i)$, where three spectral bands around $\lambda_i = 0.85$, 1.6, and 2.2 μm are selected. These bands from the near and shortwave infrared region are very sensitive to cloud shadow effects, because the direct part of the downwelling solar radiation flux at the ground level is typically 80% or more of the total downwelling flux (see figure 1).

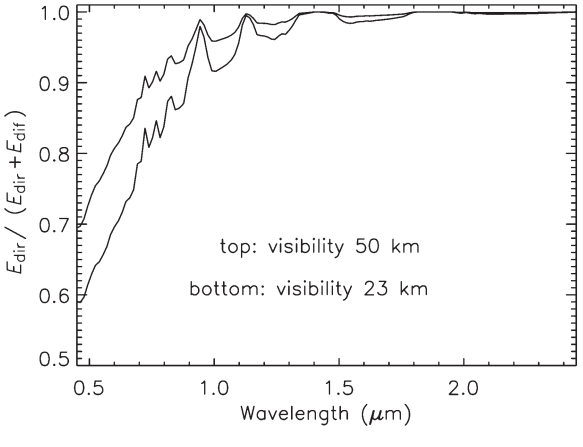

Figure 1. Ratio of direct to total downwelling solar flux at sea level for two visibilities, calculated by MODTRAN for a midlatitude summer atmosphere with a rural aerosol, solar zenith angle = 40°, and ground albedo = 0.15. The spectral resolution is 15 nm.

The graph shows the general trend of an increase of the ratio of direct to total flux with longer wavelengths. The simulation was performed with the MODTRAN (moderate resolution transmission) code (Berk *et al*. 1998, 2000) employing the midlatitude summer atmosphere with a rural aerosol, solar zenith angle of 40°, surface albedo of 0.15, and ground at sea level. The spectral resolution is 15 nm. Channels in the blue-to-red region (0.4–0.7 μm) are not used for the detection of shadow regions because they receive a much larger diffuse radiation component, making them less sensitive to partial shadow effects. In this contribution the ATCOR (atmospheric correction) code is used for the atmospheric correction (Richter 1996, 1998, Richter and Schläpfer 2002), which employs a database of radiative transfer calculations based upon MODTRAN.

The surface reflectance is first computed with the assumption of full solar illumination, i.e. the global flux on the ground consists of the direct (E_{dir}) and diffuse (E_{dif}) component. If DN denotes the digital number of a pixel, L_{P} the path radiance, and τ the atmospheric transmittance (ground-to-sensor) the surface reflectance can be obtained as (Richter 1996):

$$\rho_i(x, y) = \frac{\pi\left(d^2\{c_0(i) + c_1(i)DN_i(x, y)\} - L_{\mathrm{p},i}\right)}{\tau_i(E_{\mathrm{dir},i} + E_{\mathrm{dif},i})}. \tag{1}$$

Here, d is the Earth–sun distance at the image acquisition time in astronomical units, c_0 and c_1 are the radiometric calibration coefficients (offset and slope) to convert the digital number into the corresponding at-sensor radiance L, i.e. $L = c_0 + c_1\ DN$, and i is the channel index.

The proposed de-shadowing algorithm consists of a sequence of eight processing steps as sketched in figure 2. It starts with atmospheric correction (equation (1)). The next step is the masking of water bodies and cloud areas with simple spectral criteria

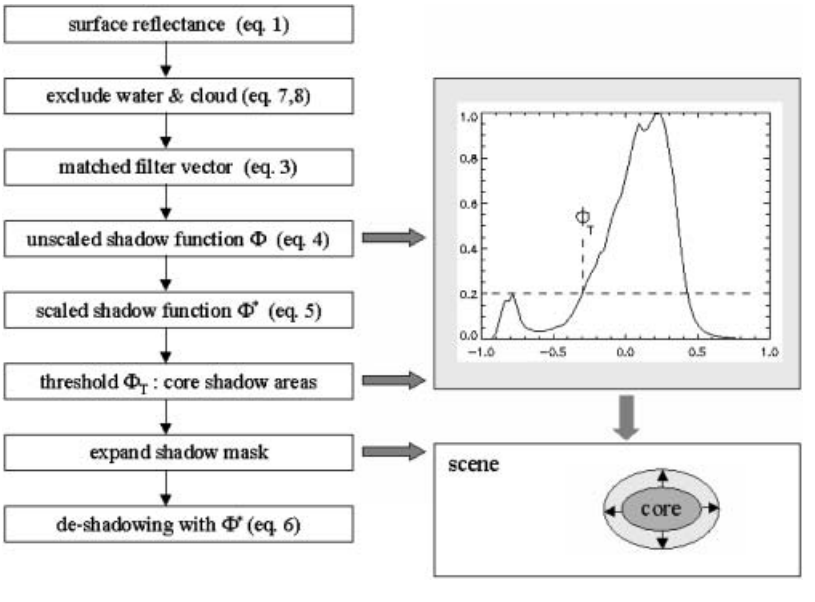

Figure 2. Processing steps of de-shadowing method.

as detailed in the discussion section. Water pixels have to be excluded as far as possible to avoid their assignment as shadow pixels; see §3.

Step 3 calculates the covariance matrix $C(\rho')$where ρ' is the reflectance vector comprising only the non-water and non-cloud pixels. For each pixel, this vector holds the reflectance values in the three selected channels (around 0.85, 1.6 and 2.2 μm). The matched filter is a vector tuned to a certain target reflectance spectrum ρ'_T to be detected (Adler-Golden *et al.* 2002):

$$V_{mf} = \frac{C^{-1}(\rho'_T - \overline{\rho}')}{(\rho'_T - \overline{\rho}')^T C^{-1}(\rho'_T - \overline{\rho}')}. \quad (2)$$

Here, $\bar{\rho}'$ is the scene-average spectrum, without the water/cloud pixels. Selecting $\rho'_T = 0$ for a shadow target yields a special simplified form of the matched filter, where the 'sh' index indicates shadow:

$$V_{sh} = -\frac{C^{-1}\overline{\rho}'}{\overline{\rho}'^T C^{-1}\overline{\rho}'}. \quad (3)$$

The shadow matched filter vector is then applied to the non-water/non-cloud part of the scene and yields the still un-normalized values of Φ, which are a relative measure of the fractional direct illumination, also called the *unscaled shadow function* here:

$$\Phi(x, y) = V_{sh}^T(\rho'(x, y) - \overline{\rho}'). \quad (4)$$

The matched filter calculates a minimum rms shadow target abundance for the entire (non-water/non-cloud) scene. Therefore, the values of Φ are positive and negative numbers. The arbitrary, image-depending range of Φ has to be rescaled to the physical range from 0 to 1, where 0 indicates no direct illumination (full shadow), and 1 means full direct illumination. The histogram of Φ is used to rescale the image data. Figure 3 shows a schematic sketch of such a histogram with a smaller peak (at Φ_2) representing the shadow pixels and the main peak (at Φ_{max}) representing the majority of the fully illuminated areas. The statistical assumption is used that full direct solar illumination is already obtained for pixels with $\Phi(x,y) = \Phi_{max}$. Then the values Φ are linearly mapped from the unscaled (Φ_{min},

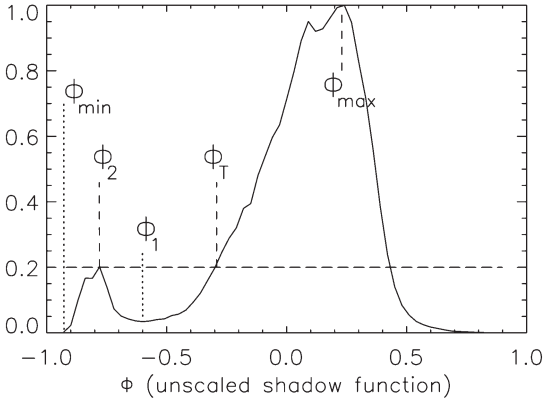

Figure 3. Normalized histogram of unscaled shadow function.

$\Phi_{\max}$) interval onto the physically scaled (0,1) interval, where the *scaled shadow function* is named Φ^*:

$$\Phi^* = \frac{\Phi - \Phi_{\min}}{\Phi_{\max} - \Phi_{\min}} \quad \text{if } \Phi \leqslant \Phi_{max} \tag{5a}$$

$$\Phi^* = 1 \quad \text{if } \Phi > \Phi_{max}. \tag{5b}$$

The smallest value of the scaled shadow function is $\Phi^*_{\min} = 0$, which means no direct illumination. However, to avoid overcorrection and to cope with scenes containing merely partial shadow areas, it is advisable to set $\Phi^*_{\min}$ at a small positive value. This value of $\Phi^*_{\min}$, i.e. the minimum fractional direct illumination (deepest shadow in a scene, typically ranging from 0.05 to 0.10) is scene-dependent; see the discussion in the next section.

In principle, the de-shadowing could now be performed with the physically scaled function Φ^*, which represents the fraction of the direct illumination for each pixel in the ρ' vector, i.e. the complete scene without cloud and water pixels. However, as mentioned in the introduction, since the matched filter is not a perfect shadow transformation, it is much better to restrict its application to the potential, most-likely shadow areas. This is an important processing step to reduce the number of misclassifications or false-alarms. If omitted it will cause strange 'shadow' pixels scattered all over the image. An example can be found in the central part of figure 4 where the standard shadow map contains a lot of artifact shadow areas.

Therefore, the proposed method tries to find the core shadow areas in a scene, and subsequently expands the core regions to obtain the final mask that includes a smooth shadow/clear transition. The physically scaled shadow function Φ^* is then applied only to the pixels in the final mask.

The histogram of the unscaled shadow function Φ can be employed to separate regions of low values of Φ from the moderate-to-high values; compare figure 3. A threshold Φ_{T} can be set in the vicinity of the local histogram minimum (Φ_1) and the core shadow mask is defined by those pixels with $\Phi(x,y) < \Phi_{\mathrm{T}}$. The details of the choice of Φ_{T} are discussed in §3. As always with thresholding, some arbitrariness is involved in the final selection.

Once the core shadow mask has been defined, it is expanded to include the surrounding shadow/clear transition zone of 100 m width. De-shadowing with the scaled shadow function $\Phi^*(x,y)$ is then exclusively applied to the pixels in this final mask. This means the direct solar flux (E_{dir} in equation (1)) has to be multiplied with $\Phi(x,y)$:

$$\rho_i(x, y) = \frac{\pi\left(d^2\{c_0(i) + c_1(i)DN_i(x, y)\} - L_{p,i}\right)}{\tau_i(E_{\mathrm{dir},i}\Phi^*(x, y) + E_{\mathrm{dif},i})}. \tag{6}$$

In equations (1) and (6) the aerosol optical depth or visibility required for the atmospheric terms (path radiance, transmittance, direct and diffuse flux) can be derived from the image provided the necessary bands in the visible and shortwave infrared region exist and the scene contains dark reference areas (Kaufman *et al.* 1997). Otherwise, the user has to specify an estimated visibility. The second important atmospheric parameter is the water vapour column. For instruments with bands in the atmospheric water vapour regions this information can be derived from the image data (Schläpfer *et al.* 1998), otherwise an estimate has to be provided by

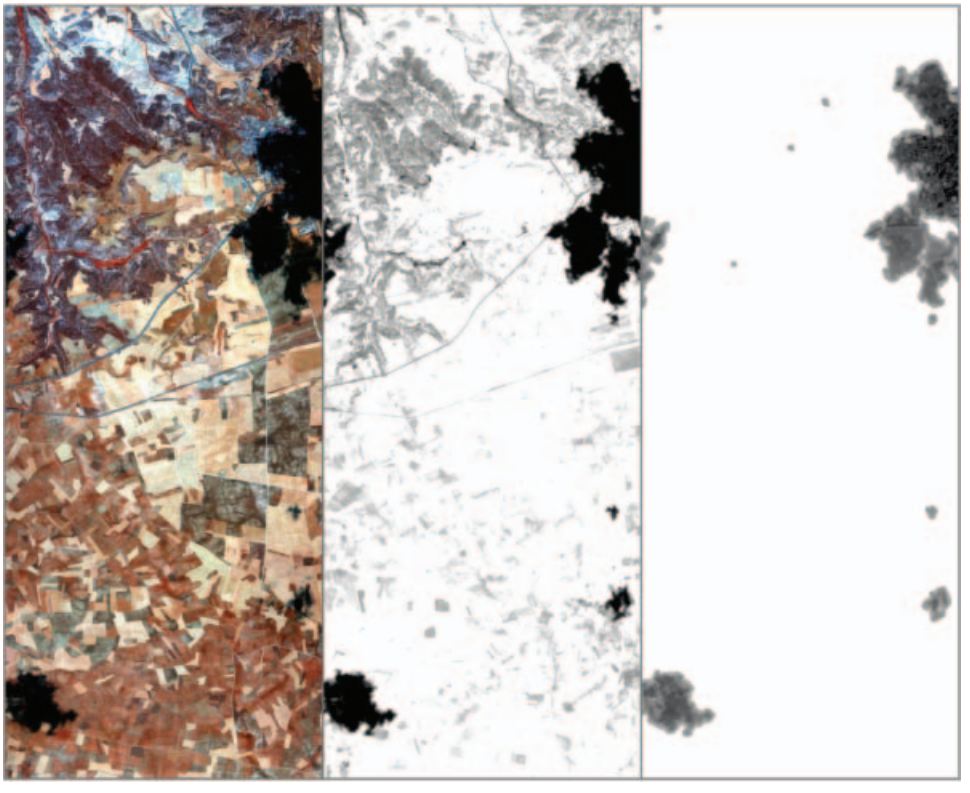

Figure 4. Left: surface reflectance image of HyMap at Chinchon, Spain (colour coding: RGB=878, 646, 462 nm channels); centre: standard shadow map showing a number of artifact shadow areas (grey patches) which do not appear with the core shadow approach (right part); right: improved cloud shadow map derived from core shadow regions.

the user. In summary, three channels (around 0.85, 1.6 and 2.2 μm) are used to define a matched filter vector with three elements per pixel. For each image pixel the surface reflectance in these three channels and the scene-average reflectance of these channels are calculated to obtain the unscaled shadow function, and finally the scaled shadow function. The same shadow function is employed to de-shadow the imagery not only in the initial three channels but also for all channels of the sensor (equation (6)).

3. Discussion of critical parameters

One of the most important parameters is the available number of spectral channels during the covariance matrix and matched filter part of the algorithm. The minimum requirement is a band in the near-infrared region (0.8–1.0 μm). The performance usually increases significantly if two additional bands (at 1.6 μm and at 2.2 μm) are available, i.e. a Landsat TM type of multispectral sensor. Even for hyperspectral imagery these three bands (around 0.85, 1.6 and 2.2 μm) are sufficient for the matched filter calculation. The usage of a hundred bands would not be helpful, but only cause numerical problems during the inversion of the covariance matrix (equation (3)).

Spectral channels from the visible region are only employed for the masking of cloud regions, not for the matched filter part, because water, vegetation, dark soils, and shadowed pixels all range within a few per cent reflectance. In addition, the visible region is not very sensitive to partial shadow effects, as shown in the lower direct radiation signal in figure 1; implying a higher diffuse component in the visible as compared to wavelengths longer than 0.8 μm.

The distinction of water bodies from cloud shadow areas may be difficult or impossible if it is based merely on spectral reflectance shape and amplitude information. Water bodies should be excluded as far as possible to improve the performance of the de-shadowing algorithm. Currently, water and cloud pixels are masked with the spectral criteria:

$$\rho(0.85\ \mu\text{m}) \leqslant 5\% \text{ and } \rho(1.6\ \mu\text{m}) \leqslant 1\% \quad \text{(water)} \tag{7}$$

$$\rho(0.48\ \mu\text{m}) \geqslant 30\% \text{ and } \rho(1.6\ \mu\text{m}) \geqslant 30\% \quad \text{(cloud)} \tag{8}$$

If no channel in the blue region is available, a channel in the green (0.5–0.6 μm) or red part of the spectrum (0.6–0.68 μm) could be used as a substitute. Both criteria do not uniquely define the corresponding class. The water criteria allow some margin for turbid water in the NIR region. The more restrictive criterion $\rho(0.85\ \mu\text{m}) < 3\%$ would perform better for clear water bodies. However, it would fail for moderately turbid or muddy waters. Other common water classification criteria such as average reflectance over all bands $\bar{\rho} \leqslant 3\%$ or $\rho(0.4\text{–}0.6\ \mu\text{m}) < 6\%$ may also fail. So one has to compromise and tolerate a certain amount of misclassification for a fully automatic algorithm. The scaled shadow map $\Phi^*(x,y)$ is written to an output file. If required, it can be edited, based on *a priori* knowledge of a user, to remove misclassified shadow areas, and an updated de-shadowing calculation could take place.

The histogram of the unscaled shadow function Φ (figure 3) typically has a main peak at $\Phi_{\max}$, a smaller secondary peak (at Φ_2) due to shadow pixels, and a local minimum (at Φ_1). The secondary peak can be determined by level-slicing the normalized histogram. We arbitrarily define a threshold Φ_T as the intersection of this slice line at the level of $h(\Phi_2)$ with the normalized histogram $h(\Phi)$ for $\Phi_1 < \Phi < \Phi_{\max}$; see figure 3. The approach with a main peak and a smaller secondary peak is restricted to cases where the percentage of shadow pixels in the scene is less than about 25%, otherwise the method fails. This is appropriate for satellite scenes, since imagery with a cloud cover of more than 25% is usually not delivered to customers. If the secondary peak at Φ_2 is not clearly defined numerically, i.e. no local minimum found at Φ_1, or histogram difference $h(\Phi_2) - h(\Phi_1) < 0.03$, then Φ_T is defined as the intersection of the slice level 0.10 with $h(\Phi)$ for $\Phi < \Phi_{\max}$.

Masking of the core shadow areas with $\Phi < \Phi_T$ (see figure 3) is critical, like any thresholding process: a large threshold could potentially include non-shadow areas, and a low threshold could miss shadow areas. The current automatic algorithm has the three user-selectable options of a small, medium or large core shadow mask corresponding to thresholds set at $\Phi_T - 0.1$, Φ_T, and $\Phi_T + 0.1$, respectively. The default value for the fully automatic algorithm is the medium-size mask.

A second tunable parameter is the minimum fractional direct illumination $\Phi^*_{\min}$, also called depth of shadow. Theoretically, $\Phi^*_{\min}$ can be zero, i.e. a completely shadowed pixel receiving only diffuse solar illumination. However, a too low estimate close to zero will boost the surface reflectance, especially for channels in the 1.5–2.5 μm region (equation (6)), since the diffuse solar radiation term E_{dif} is very

small. Therefore, small positive values of $\Phi^*_{\min}$ are recommended. The range of $\Phi^*_{\min}$ is typically 0.05–0.1, with the default set at $\Phi^*_{\min} = 0.08$.

The proposed automatic method was successfully tested on dozens of scenes covering different climates and landscapes. However, there will always be situations where interactive methods are superior, because a human operator includes additional *a priori* knowledge not contained in a spectral scene. Still, a certain flexibility is included in our technique because two parameters are tunable, namely the threshold Φ_T for the size of the core shadow mask and the shadow depth $\Phi_{\min}$.

The advantage of the presented method is its fast processing performance, because it relies exclusively on spectral calculations and avoids time-consuming geometric cloud/shadow pattern considerations. The drawback is that useful geometric information is neglected. Future improvements of the method could include the consideration of digital elevation model (DEM) effects, such as the sky view factor (Dozier *et al*. 1981, Richter 1998), to account for the effective fraction of the diffuse skylight from the visible part of the sky dome.

4. Examples of de-shadowing imagery

Three selected examples show the performance of the method under different climatic conditions and landscapes. We consider a semi-arid climate scene in Spain, a tropical rain forest area in Kenya, and a mid-European scene with agricultural areas and a lot of inland lakes.

4.1 *Hyperspectral airborne scene (Spain)*

The first example of processing (figure 4, left) demonstrates a successful shadow removal for a situation where all clouds are outside the airborne scene, so a cloud shadow algorithm relying on cloud patterns would fail. The imagery was recorded by the HyMap sensor (Hyperspectral Mapper, Cocks *et al*. 1998). It is a subset with 1250 scan lines acquired at Chinchon, Spain, 12 July 2003, 12:10 h UTC. The geographic coordinates are latitude 40°3′ N, longitude 3°21′ W. The flight altitude was 4 km, heading 196°, solar zenith angle 18.3°, and solar azimuth 173.5°. The 2003 version of the HyMap instrument covers the 0.45–2.45 μm spectral region with 126 bands.

Figure 4 (left) shows the atmospherically corrected surface reflectance image prior to de-shadowing. The centre of the figure presents the standard shadow map employing all image pixels. Figure 4 (right) is the corresponding improved shadow map derived from the core shadow areas. Obviously, the standard shadow map contains a lot of misclassified pixels (grey areas), such as roads, borders between different fields, and others. The improved shadow map also contains some small artifact areas, but it has a much lower number of misclassified pixels. It nicely captures the significant shadow areas. Figure 5 shows a zoomed view from the top of this scene. It presents reflectance data before de-shadowing, and results after de-shadowing with the standard and core-shadow method. A comparison immediately reveals the superior performance of the new method in the marked regions A, B, C, D, and in the dark shadow areas. The marked domains contain example areas where the standard procedure wrongly assigns shadow pixels (compare figure 4) which are not included in the improved method.

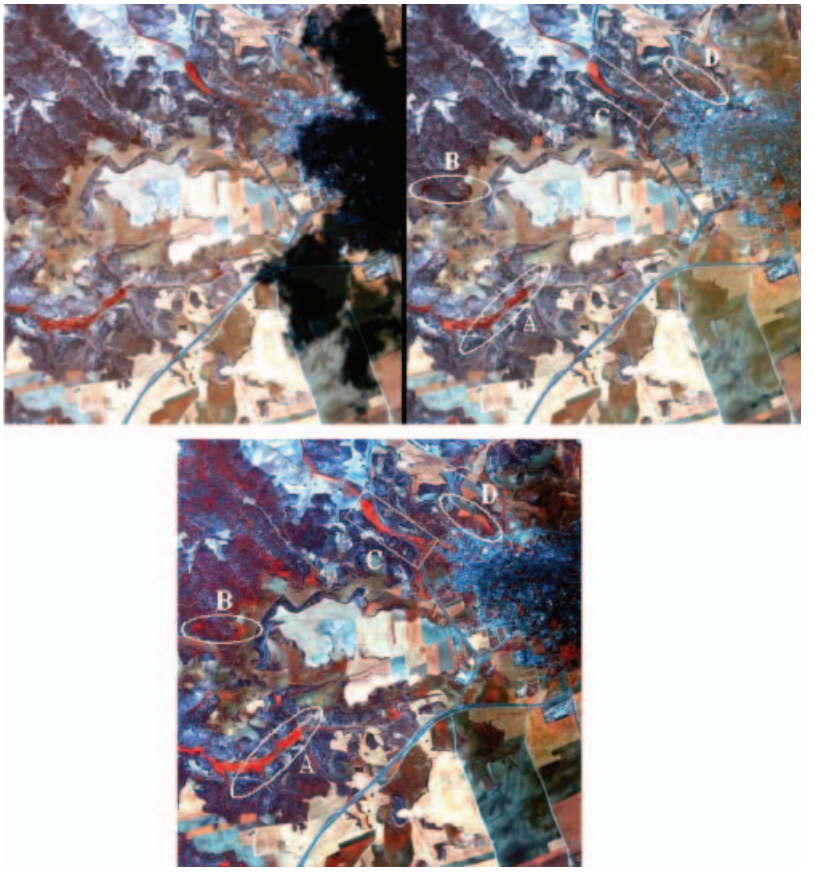

Figure 5. Zoomed view of figure 4. Top left: reflectance image assuming full illumination; top right: after de-shadowing using the core shadow approach; bottom: after standard de-shadowing employing the entire image.

4.2 *Landsat ETM+ scene from Kenya*

The second scene is a subset of Landsat 7 ETM+ imagery from western Kenya (path/row=170/60), latitude 0°13′ N, longitude 34°37′ E. The scene was acquired on 10 April 2001, and mainly contains tropical rain forests. The solar zenith angle is 30.7°, and solar azimuth 74.2°. Figure 6 (top) shows an overview of selected subscene. At the bottom a zoomed view of the reflectance data before and after de-shadowing is presented. Figure 7 shows two surface reflectance spectra retrieved from the position marked with an arrow. The lower curve is the spectrum from the cloud shadow area, calculated with the assumption of a full solar illumination, and the upper one represents de-shadowed data. The de-shadowed reflectance spectrum is within the typical range of forest vegetation spectra from this region.

4.3 *Landsat ETM+ scene from Germany*

The third example is a subset of Landsat 7 ETM+ imagery from Germany, north-west of Berlin (path/row=194/23), acquired 1 May 2000. The solar zenith angle is 41°, and solar azimuth 154.9°. The area represents central European landscapes,

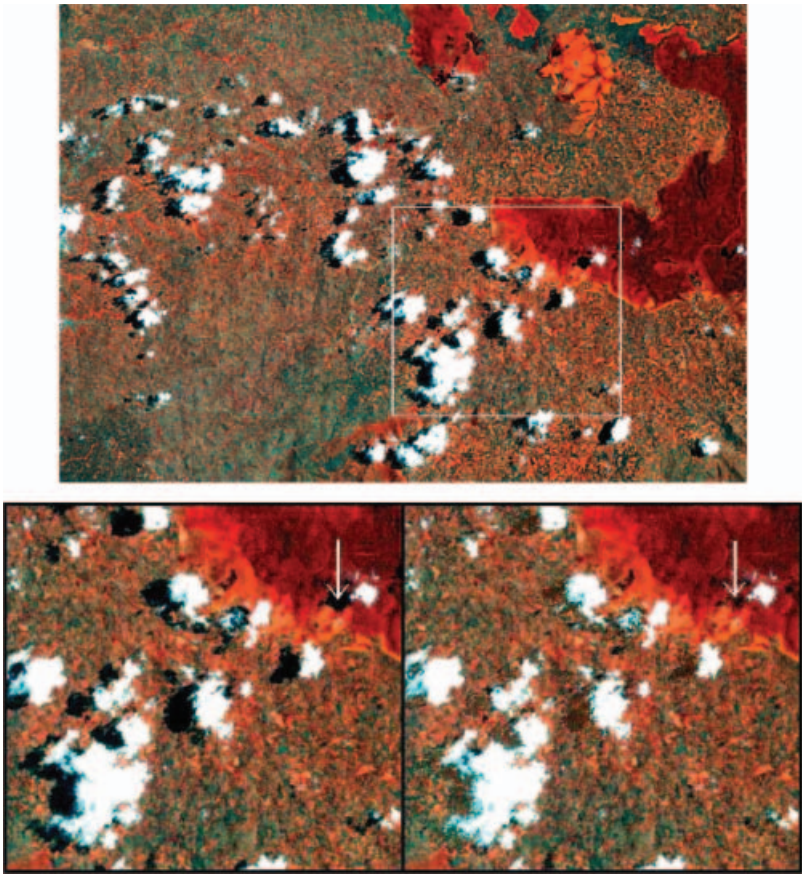

Figure 6. Landsat ETM+ subscene from Kenya. Top: overview; bottom: zoomed view before and after de-shadowing. Colour coding: RGB=bands 4/2/1 (830, 560, 480 nm). The images are atmospherically corrected surface reflectance data.

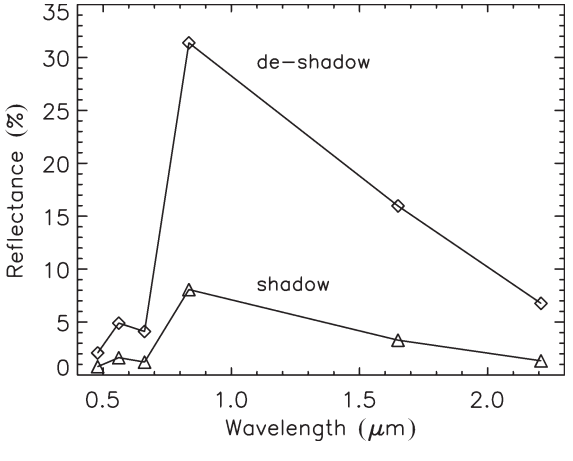

Figure 7. Vegetation spectrum from figure 6 before and after de-shadowing.

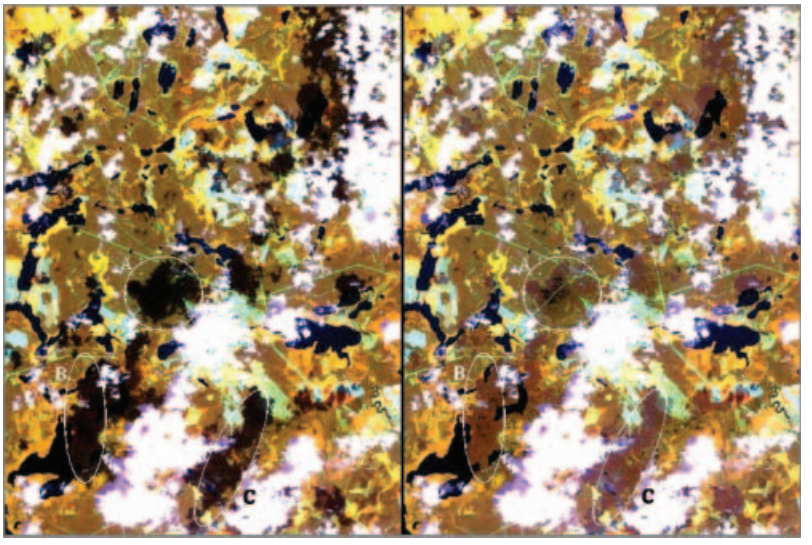

Figure 8. Landsat ETM+ subscene from Germany before (left) and after (right) de-shadowing. Colour coding: RGB=bands 4/5/3 (830, 1650, 660 nm). The images are atmospherically corrected surface reflectance data.

mostly agricultural areas with a lot of lakes. The cloud cover is about 20%. De-shadowing is particularly difficult in this scene, because the lake bodies are often murky, or contain reed areas, so they can easily be misinterpreted as land regions. Based upon topographic maps, it is estimated that about 20% of the pixels assigned as land shadow areas are water bodies in reality, mostly small lakes and lake border regions. Still, many true land details hidden in shadow areas of the uncorrected scene can be clearly seen in the de-shadowed image, see the areas marked A, B, C, in figure 8.

5. Summary

A fully automatic de-shadowing method for spectral imagery has been developed, requiring at least a visible and a near-infrared channel. Essential parts of the technique are the scaled shadow function and the concept of core shadow and expanded shadow regions to reduce the number of shadow-pixel misclassifications significantly as compared to the standard method. The algorithm was implemented with two tunable parameters: the size of the core shadow mask (small, medium, large) and the minimum fractional direct solar illumination of the darkest shadow areas, the depth of shadow. Once the parameters have been set the algorithm runs fully automatically. Default values are provided that usually yield good de-shadowing results. However, for optimum performance these two parameters might have to be tuned depending on the scene. The method is restricted to scenes where the percentage of cloud coverage is less than 25%. It was successfully applied to multispectral satellite scenes and hyperspectral airborne imagery.

References

Adler-Golden, S.M., Matthew, M.W., Anderson, G.P., Felde, G.W. and Gardner, J.A., 2002, An algorithm for de-shadowing spectral imagery. In

Proceedings of the 11th JPL Airborne Earth Science Workshop, 5–8 March 2002 (Pasadena, USA: JPL Publication 03–04).

BERK, A., BERNSTEIN, L.S., ANDERSON, G.P., ACHARYA, P.K., ROBERTSON, D.C., CHETWYND, J.H. and ADLER-GOLDEN, S.M., 1998, MODTRAN cloud and multiple scattering upgrades with application to AVIRIS. *Remote Sensing of Environment*, **65**, pp. 367–375.

BERK, A., ANDERSON, G.P., ACHARYA, P.K., CHETWYND, J.H., BERNSTEIN, L.S., SHETTLE, E.P., MATTHEW, M.W. and ADLER-GOLDEN, S.M., 2000, *MODTRAN4 Users' Manual*. Air Force Research Laboratory, Hanscom AFB, MA, USA.

BOARDMAN, J.W., 1993, Automated spectral unmixing of AVIRIS data using convex geometry concepts. In *Summaries of Fourth JPL Airborne Geoscience Workshop*, 25–29 October, 1993, Washington (Pasadena, USA: JPL Publication 95-26, v.1), pp. 11–14.

COCKS, T., JENSSEN, R., STEWART, A., WILSON, I. and SHIELDS, T., 1998, The HyMap airborne hyperspectral sensor: the system, calibration and performance. *First EARSeL Workshop on Imaging Spectroscopy*, 6–8 October 1998, Zurich, Switzerland (Paris: EARSeL), pp. 37–42.

DOZIER, J., BRUNO, J. and DOWNEY, P., 1981, A faster solution to the horizon problem. *Computers & Geosciences*, **7**, pp. 145–151.

KAUFMAN, Y.J., WALD, A.E., REMER, L.A., GAO, B.-C., LI, R.R. and FLYNN, L., 1997, The MODIS 2.1 μm channel – correlation with visible reflectance for use in remote sensing of aerosol. *IEEE Transactions on Geoscience and Remote Sensing*, **35**, pp. 1286–1297.

POOR, H.V., 1983, Robust matched filters. *IEEE Transactions on Information Theory*, **IT-29**, pp. 677–687.

RICHTER, R., 1996, A spatially adaptive fast atmospheric correction algorithm. *International Journal of Remote Sensing*, **17**, pp. 1201–1214.

RICHTER, R., 1998, Correction of satellite imagery over mountainous terrain. *Applied Optics*, **37**, pp. 4004–4015.

RICHTER, R. and SCHLÄPFER, D., 2002, Geo-atmospheric processing of airborne imaging spectrometry data. Part 2: atmospheric/topographic correction. *International Journal of Remote Sensing*, **23**, pp. 2631–2649.

SCHLÄPFER, D., BOREL, C.C., KELLER, J. and ITTEN, K.I., 1998, Atmospheric precorrected differential absorption technique to retrieve columnar water vapor. *Remote Sensing of Environment*, **65**, pp. 353–366.

SIMPSON, J.J. and STITT, J.R., 1998, A procedure for the detection and removal of cloud shadow from AVHRR data over land. *IEEE Transactions on Geoscience and Remote Sensing*, **36**, pp. 880–897.

TURIN, G.L., 1975, Minimax strategies for matched-filter detection. *IEEE Transactions on Communications*, **COM-23**, pp. 1370–1371.

TURIN, G.L., 1976, An introduction to digital matched filters. *Proceedings of IEEE*, **64**, pp. 1092–1112.